Tamás G. Molnár
Department of Applied Mechanics,
Budapest University of
Technology and Economics,
Budapest 1111, Hungary
e-mail: molnar@mm.bme.hu

Tamás Insperger
Department of Applied Mechanics,
Budapest University of
Technology and Economics,
Budapest 1111, Hungary
e-mail: insperger@mm.bme.hu

S. John Hogan
Department of Engineering Mathematics,
University of Bristol,
Bristol BS8 1TH, UK
e-mail: s.j.hogan@bristol.ac.uk

Gábor Stépán
Department of Applied Mechanics,
Budapest University of
Technology and Economics,
Budapest 1111, Hungary
e-mail: stepan@mm.bme.hu

Estimation of the Bistable Zone for Machining Operations for the Case of a Distributed Cutting-Force Model

Regenerative machine tool chatter is investigated for a single-degree-of-freedom model of turning processes. The cutting force is modeled as the resultant of a force system distributed along the rake face of the tool, whose magnitude is a nonlinear function of the chip thickness. Thus, the process is described by a nonlinear delay-differential equation, where a short distributed delay is superimposed on the regenerative point delay. The corresponding stability lobe diagrams are computed and are shown numerically that a subcritical Hopf bifurcation occurs along the stability boundaries for realistic cutting-force distributions. Therefore, a bistable region exists near the stability boundaries, where large-amplitude vibrations (chatter) may arise for large perturbations. Analytical formulas are obtained to estimate the size of the bistable region based on center manifold reduction and normal form calculations for the governing distributed-delay equation. The locally and globally stable parameter regions are computed numerically as well using the continuation algorithm implemented in DDE-BIFTOOL. The results can be considered as an extension of the bifurcation analysis of machining operations with point delay.
[DOI: 10.1115/1.4032443]

Keywords: metal cutting, turning, delay-differential equation, distributed delay, Hopf bifurcation, center manifold reduction, bistable zones

1 Introduction

Suppressing or avoiding harmful vibrations (chatter) during machining is very important in terms of increasing the accuracy and productivity of metal cutting processes. Machine tool chatter has many unfavorable effects: it reduces the surface quality, limits productivity, increases tool wear, produces noise, and may even damage the tool. One of the most accepted explanations for machine tool chatter is the so-called surface regeneration effect [1,2]: the machined surface becomes wavy due to the relative vibrations between the tool and the workpiece, and the surface waviness excites the oscillations of the machine tool-workpiece system in the subsequent cut. Hence, the surface waviness is regenerated during consecutive cuts and vibrations amplify in a self-excited manner. This phenomenon can be described by delay-differential equations. Chatter corresponds to a large-amplitude oscillating solution of this equation. Based on the stability analysis of the stationary motion, so-called stability lobe diagrams can be created, which identify the chatter-free parameter domains on the plane of the spindle speed and the depth of cut. These stability charts help in the choice of technological parameters associated with optimal material removal rate.

In this paper, we present stability lobe diagrams of orthogonal turning operations. According to the experimental results, see, e.g., Refs. [3–5], the stability lobes tend to shift upward at low spindle speeds. One possible explanation for this phenomenon is the concept of process damping: the increased stability is due to an additional damping force inversely proportional to the spindle speed. According to Refs. [3–6], this additional damping force originates from the interference of the tool flank with the wavy surface of the workpiece. According to the model described in

Ref. [6], this force is also due to the dependence of the instantaneous chip thickness on the vibration velocity of the cutting tool. An alternative explanation of the same phenomenon is the so-called short regenerative effect [7,8]: the interface between the tool and the chip is represented by a finite contact surface, and the cutting force is modeled as the resultant of a force system distributed along the rake face of the tool. Since the chip needs a certain amount of time to slip along the tool, an additional (short) distributed delay is introduced in the model equations. Although the distributed delay is significantly shorter than the regenerative delay, it may result in qualitative changes in the stability lobe diagrams. Thus, the change in the stability properties at low spindle speeds can be described by a multiscale mechanism: by the interplay of a large point delay and the short distributed delay.

In this paper, we extend the model of Ref. [7] and investigate the short regenerative effect for orthogonal cutting taking the nonlinearity of the cutting-force characteristics into account. Section 2 describes the investigated mechanical model and derives the governing delay-differential equation. Section 3 explains the results of the linear stability analysis and shows the occurrence of a Hopf bifurcation at the stability boundaries. In Sec. 4, center manifold reduction and normal form calculations are carried out to estimate the amplitude and stability of the periodic orbit arising from the Hopf bifurcation. Section 5 shows that a bistable region exists near the stability boundaries, where two stable solutions, stationary cutting and large-amplitude chatter coexist. Here, an analytical estimate is given for the size of the bistable region, which is also determined numerically in Sec. 6 using DDE-BIFTOOL [9,10]. The main results are summarized in Sec. 7.

2 Mechanical Model

The single-degree-of-freedom model of turning operations shown in Fig. 1 is investigated. This model with linear cutting-force expression has already been investigated in Ref. [7]. Now we extend the model of Ref. [7] considering a nonlinear cutting-
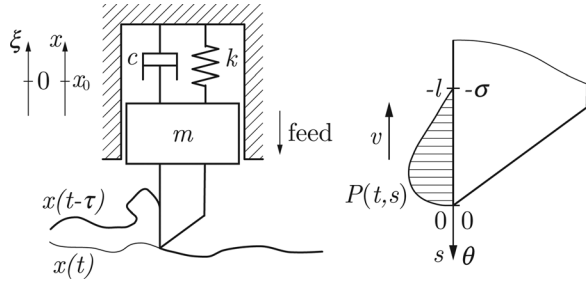
Copyright © 2016 by ASME

Fig. 1 Single-degree-of-freedom model of turning operations with distributed cutting force

force characteristics. The differential equation governing the tool motion assumes the form

$$m\ddot{x}(t) + c\dot{x}(t) + kx(t) = F_x(t) \qquad (1)$$

where m, c, and k are the modal mass, damping, and stiffness parameters, respectively, and $F_x(t)$ is the x-directional cutting-force component acting on the tool.

2.1 Cutting-Force Models. We follow the model of Ref. [7], where the linear stability of cutting processes with distributed cutting force was analyzed. We model the cutting force $F_x(t)$ as the resultant of a force system $P_x(t, s)$ distributed along the rake face of the tool on the chip-tool contact region of size l (cf. Fig. 1). We use the local coordinate $s \in [-l, 0]$ to describe the cutting-force distribution, and assume that $P_x(t, s)$ can be decomposed into a time-dependent magnitude $F_x^{\mathrm{T}}(t, s)$ and a time-independent weight function $W(s)$

$$F_x(t) = \int_{-l}^{0} P_x(t, s)\mathrm{d}s = \int_{-l}^{0} F_x^{\mathrm{T}}(t, s)W(s)\mathrm{d}s \qquad (2)$$

This assumption was verified experimentally for stable stationary cutting using a split-tool [11,12] and using a sapphire tool [13]. We also assume that this decomposition is valid in the case of small perturbations around the stationary cutting.

Furthermore, we assume that the chip slips along the rake face of the tool with the constant cutting speed v, which can be expressed in terms of the workpiece diameter D and the angular velocity Ω of the workpiece: $v = \Omega D/2$. Hence, we introduce the local temporal coordinate $\theta = s/v$, $\theta \in [-\sigma, 0]$, and rewrite Eq. (2) in the form

$$F_x(t) = \int_{-\sigma}^{0} F_x^{\mathrm{T}}(t, v\theta)w(\theta)\mathrm{d}\theta \qquad (3)$$

where $\sigma = l/v$ is the time it takes for a given particle of the chip to travel the distance l, and the weight function $w(\theta) = vW(v\theta)$ characterizing the shape of force distribution along the rake face is normalized so that

$$\int_{-\sigma}^{0} w(\theta)\mathrm{d}\theta = 1 \qquad (4)$$

The magnitude $F_x^{\mathrm{T}}(t, v\theta)$ of the cutting-force distribution is related to the uncut chip thickness $h(t, \theta)$ by the cutting-force characteristics. The two most widely accepted characteristics are the power law (or Taylor force) [14] and the cubic characteristics (or Tobias force) [15], but other functions are also used, see Ref. [16] and the references therein. The Taylor force can be given in the form

$$F_x^{\mathrm{Taylor}}(t, v\theta) = \begin{cases} Ka_p h^q(t, \theta) & \text{if } h(t, \theta) \geq 0 \\ 0 & \text{if } h(t, \theta) < 0 \end{cases} \qquad (5)$$

where K is the measured cutting coefficient, $q = 3/4$ is the cutting exponent, a_p is the chip width. The Tobias force expression reads

$$F_x^{\mathrm{Tobias}}(t, v\theta) = \begin{cases} a_p(\rho_1 h(t, \theta) + \rho_2 h^2(t, \theta) + \rho_3 h^3(t, \theta)) & \text{if } h(t, \theta) \geq 0 \\ 0 & \text{if } h(t, \theta) < 0 \end{cases} \qquad (6)$$

where the following constants were identified in the experiments reported in Ref. [15] for a milling tool of four teeth: $\rho_1 = 6.1096 \times 10^9\,\mathrm{N/m^2}$, $\rho_2 = -5.41416 \times 10^{13}\,\mathrm{N/m^3}$, and $\rho_3 = 2.03769 \times 10^{17}\,\mathrm{N/m^4}$.

The two force characteristics can be seen in Fig. 2. Both functions are nonlinear and monotonously increasing for positive chip thickness $h(t, \theta) > 0$, and are zero for negative chip thickness $h(t, \theta) < 0$, that is, when the tool loses contact with the workpiece during large-amplitude chatter. In this work, however, we exclude the latter case and assume $h(t, \theta) \geq 0$ during the entire machining operation.

2.2 Instantaneous Chip Thickness. According to the theory of regenerative machine tool vibrations, the instantaneous chip thickness $h(t, \theta)$ can be given as a function of the tool position at the actual and the previous cut

$$h(t, \theta) = h_0 + x(t - \tau + \theta) - x(t + \theta), \quad \theta \in [-\sigma, 0] \qquad (7)$$

where h_0 is the prescribed (mean) chip thickness and τ is the regenerative delay, which now equals the rotational period: $\tau = 2\pi/\Omega$. Note that the argument of the tool position is shifted by θ to account for the short time the chip needs to slip along the rake face from the tip to the position s.

2.3 Cutting-Force Distribution. The shape $w(\theta)$ of the cutting-force distribution can be determined from the literature on normal and shear stress distributions along the chip–tool interface, see Refs. [17–19] and the references therein. In our model, we use the x-directional component of the cutting force, which, in case of zero rake angle, is the resultant of the shear stress. According to Refs. [6,11,12,20,21], the shear stress S has a plateau near the tool tip and then decays to zero at the end of contact, see Fig. 3(a). Whereas in Refs. [13,22], it was shown that the shear stress S increases from a small value at the tip to a maximum $S_{\max}$, and then decays, cf. Fig. 3(b).

Since the majority of the literature describes the shear stress using the plateau-and-decay distribution, we investigate the distribution of Fig. 3(a), where chip–tool interface consists of a sticking region with constant shear stress and a sliding region with decaying stresses. Accordingly, we approximate the shape of force distribution by
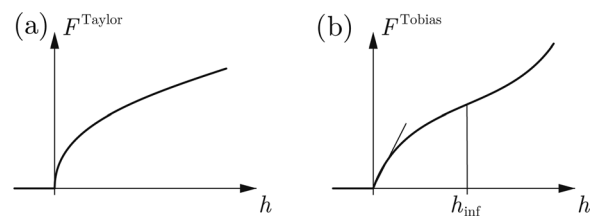

Fig. 2 Force characteristics of two different cutting-force models: Taylor force (a) and Tobias force (b)
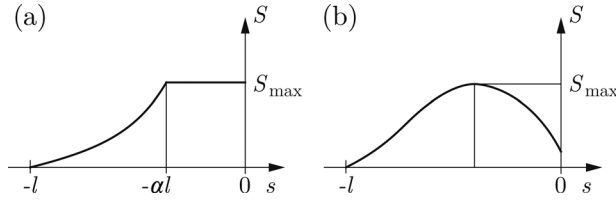
Fig. 3 Distribution of the shear stress along the rake face of the tool

$$w(\theta) = \begin{cases} \dfrac{1}{\sigma}\dfrac{1-\mathrm{e}^{-\alpha+1}}{2-(\alpha+1)\mathrm{e}^{-\alpha+1}} & \text{if } \theta \in [-\alpha\sigma, 0] \\[2mm] \dfrac{1}{\sigma}\dfrac{1-\mathrm{e}^{\theta/\sigma+1}}{2-(\alpha+1)\mathrm{e}^{-\alpha+1}} & \text{if } \theta \in [-\sigma, -\alpha\sigma) \end{cases} \quad (8)$$

where $\alpha = l_\mathrm{s}/l$ is the sticking length to contact length ratio. This formula is a suitable approximation of the usual force distributions with a reasonable number of parameters. According to the experiments reported in Refs. [11,12,20,23], $\alpha = 0.3$–0.6. Note that $w(\theta)$ in Eq. (8) satisfies condition (4).

It is important to emphasize that the magnitude (5) and (6) and the shape (8) of the cutting-force distribution also depends on the spindle speed Ω. This dependency is not included in Eqs. (5), (6) and (8). Thus, our model does not include phenomena such as built-up edge formation and is therefore valid only for quasi-stationary changes in the spindle speed or in narrow spindle speed ranges where the contact conditions do not vary significantly. Wide spindle speed ranges can be analyzed by repeatedly modifying the parameters in Eqs. (5), (6) and (8) according to the spindle speed. Furthermore, our model assumes constant sliding speed v along the rake face. Nonuniform sliding speeds can also be modeled by scaling the kernel function according to v.

2.4 Third-Order Form of the Equation of Motion. Equation (1) can be divided by m and written as

$$\ddot{x}(t) + 2\zeta\omega_\mathrm{n}\dot{x}(t) + \omega_\mathrm{n}^2 x(t) = \frac{1}{m}F_x(t) \quad (9)$$

where $\omega_\mathrm{n} = \sqrt{k/m}$ is the natural angular frequency of the undamped system and $\zeta = c/(2\sqrt{km})$ is the damping ratio. Note that Eq. (9) is nonlinear in x through $F_x(t)$. The chatter-free stationary cutting is associated with the equilibrium $x(t) \equiv x_0 = F_0/(m\omega_\mathrm{n}^2)$, where $F_0 = Ka_\mathrm{p}h_0^q$ for the Taylor and $F_0 = a_\mathrm{p}(\rho_1 h_0 + \rho_2 h_0^2 + \rho_3 h_0^3)$ for the Tobias force expression.

In order to investigate machine tool chatter, we shift our coordinate to the equilibrium and use the perturbation $\xi(t) = x(t) - x_0$. The instantaneous chip thickness expressed in terms of $\xi(t)$ reads

$$h(t, \theta) = h_0 + \xi(t - \tau + \theta) - \xi(t + \theta), \quad \theta \in [-\sigma, 0] \quad (10)$$

whereas the equation of motion becomes

$$\ddot{\xi}(t) + 2\zeta\omega_\mathrm{n}\dot{\xi}(t) + \omega_\mathrm{n}^2\xi(t) = \frac{1}{m}\int_{-\sigma}^{0}\Delta F_x^\mathrm{T}(t, v\theta)w(\theta)\mathrm{d}\theta \quad (11)$$

Here, $\Delta F_x^\mathrm{T}(t, v\theta) = F_x^\mathrm{T}(t, v\theta) - F_0$ denotes the variation of the cutting-force magnitude, which can be approximated by the third-order polynomial

$$\begin{aligned} \Delta F_x^\mathrm{T}(t, v\theta) \approx\ & k_1(\xi(t - \tau + \theta) - \xi(t + \theta)) \\ & + k_2(\xi(t - \tau + \theta) - \xi(t + \theta))^2 \\ & + k_3(\xi(t - \tau + \theta) - \xi(t + \theta))^3, \quad \theta \in [-\sigma, 0] \end{aligned} \quad (12)$$

In the case of the Taylor force, we get this polynomial by the Taylor expansion of Eq. (5) up to third order with respect to $h(t, \theta)$ around h_0. The corresponding coefficients are

$$k_1 = \frac{3}{4}Ka_\mathrm{p}h_0^{-1/4}, \quad k_2 = -\frac{1}{8h_0}k_1, \quad k_3 = \frac{5}{96h_0^2}k_1 \quad (13)$$

For the Tobias force, substitution of Eq. (10) into Eq. (6) yields the cubic polynomial form (12) without approximation. Here, the coefficients are

$$\begin{aligned} k_1 &= a_\mathrm{p}(\rho_1 + 2\rho_2 h_0 + 3\rho_3 h_0^2) \\ k_2 &= a_\mathrm{p}(\rho_2 + 3\rho_3 h_0) \\ k_3 &= a_\mathrm{p}\rho_3 \end{aligned} \quad (14)$$

Note that the third order form is required for the subsequent bifurcation analysis.

Based on Eqs. (11) and (12), the tool motion is governed by an autonomous nonlinear differential equation with distributed delay. The kernel $w(\theta)$ of the distributed delay term originates in the shape of force distribution along the tool's rake face. The distributed delay is of length σ, and is superimposed on the regenerative point delay τ. In this study, the ratio of the two delays is assumed to be constant

$$\sigma = \varepsilon\tau \quad (15)$$

Note that the ratio $\varepsilon = l/(D\pi)$ and hence is equivalent to the ratio of the contact length l and the perimeter $D\pi$ of the workpiece, since $\sigma = l/v$, $v = \Omega D/2$, and $\tau = 2\pi/\Omega$. Therefore, ε can also be determined during stress distribution measurements along the rake face. According to Refs. [11,12], the ratio ε typically ranges between 0.0005 and 0.05. Since the point delay τ is called the regenerative delay, we refer to the additional σ-long distributed delay as the *short regenerative delay*, while its influence on the dynamics of the process is called the *short regenerative effect*.

We now write Eqs. (11) and (12) in dimensionless form. We introduce the dimensionless time $\tilde{t} = \omega_\mathrm{n}t$, and replace temporal derivatives by dimensionless ones indicated by prime according to the rule $\dot{\square} = \mathrm{d}\square/\mathrm{d}t = \omega_\mathrm{n}\mathrm{d}\square/\mathrm{d}\tilde{t} = \omega_\mathrm{n}\square'$. In a similar manner, we introduce the dimensionless delays $\tilde{\tau} = \omega_\mathrm{n}\tau$ and $\tilde{\sigma} = \omega_\mathrm{n}\sigma$, as well as the dimensionless local temporal coordinate $\tilde{\theta} = \omega_\mathrm{n}\theta$, $\tilde{\theta} \in [-\tilde{\sigma}, 0]$. We also rescale $w(\theta)$ as $\tilde{w}(\tilde{\theta}) = w(\omega_\mathrm{n}\theta)/\omega_\mathrm{n}$ and $\xi(t)$ as $\tilde{\xi}(\tilde{t}) = \xi(t)/h_0$. After dropping the tilde the governing equation reads

$$\begin{aligned} \xi''(t) &+ 2\zeta\xi'(t) + \xi(t) \\ &= p\int_{-\sigma}^{0}[(\xi(t - \tau + \theta) - \xi(t + \theta)) \\ &\quad + \eta_2(\xi(t - \tau + \theta) - \xi(t + \theta))^2 \\ &\quad + \eta_3(\xi(t - \tau + \theta) - \xi(t + \theta))^3]w(\theta)\mathrm{d}\theta \end{aligned} \quad (16)$$

where $p = k_1/(m\omega_\mathrm{n}^2)$ is the dimensionless chip width being proportional to the actual chip width a_p. The dimensionless cutting-force coefficients η_2 and η_3 are expressed in the form

$$\eta_2 = \frac{k_2}{k_1}h_0 = \begin{cases} -\dfrac{1}{8} & \text{Taylor force} \\[3mm] \dfrac{\rho_2 h_0 + 3\rho_3 h_0^2}{\rho_1 + 2\rho_2 h_0 + 3\rho_3 h_0^2} & \text{Tobias force} \end{cases} \quad (17)$$

$$\eta_3 = \frac{k_3}{k_1}h_0^2 = \begin{cases} \dfrac{5}{96} & \text{Taylor force} \\[3mm] \dfrac{\rho_3 h_0^2}{\rho_1 + 2\rho_2 h_0 + 3\rho_3 h_0^2} & \text{Tobias force} \end{cases} \quad (18)$$

Note that the coefficients η_2 and η_3 are functions of the mean chip thickness h_0 only in the case of the Tobias force. They are constant for the Taylor force.

The linear part of Eq. (16) has already been introduced in Ref. [7], and a nonlinear equation corresponding to Eq. (16) without

distributed delay but with point delay was investigated in Ref. [24]. Secs. 3–5 discuss the stability and bifurcation analysis of Eq. (16) where both the nonlinearity and the distributed delay term are included.

3   Linear Stability Analysis

Linearizing Eq. (16) around the trivial solution $\xi(t) \equiv 0$ yields

$$\xi''(t) + 2\zeta\xi'(t) + \xi(t)$$
$$= p\int_{-\sigma}^{0}[\xi(t - \tau + \theta) - \xi(t + \theta)]w(\theta)\mathrm{d}\theta \qquad (19)$$

The stability of Eq. (19) was analyzed in Ref. [7]. It was shown that an Hopf bifurcation occurs at the stability boundaries, which gives rise to oscillations at a well-defined dimensionless angular frequency ω. Note that a fold bifurcation cannot happen in this system. In Ref. [7], the D-subdivision method was used to derive the linear stability boundaries, which are parameterized by

$$\psi = \omega\tau \qquad (20)$$

Note that parameter ψ has physical meaning: it represents the phase shift between the waves on the machined surface cut momentarily and those cut one revolution ago. The stability boundaries can be given in the form

$$\omega(\psi) = -\zeta\frac{R_0(\psi)}{S_0(\psi)} + \sqrt{\zeta^2\frac{R_0^2(\psi)}{S_0^2(\psi)} + 1}$$

$$p_{\mathrm{st}}(\psi) = -\frac{2\zeta\omega(\psi)}{S_0(\psi)} \qquad (21)$$

$$\Omega(\psi) = \frac{2\pi}{\tau(\psi)} = \frac{2\pi\omega(\psi)}{\psi}$$

where $R_0(\psi)$ and $S_0(\psi)$ are the following integral terms:

$$R_0(\psi) = \int_{-\sigma}^{0}[\cos(\omega\theta) - \cos(\omega(\theta - \tau))]w(\theta)\mathrm{d}\theta = \frac{\omega^2(\psi) - 1}{p_{\mathrm{st}}(\psi)}$$

$$S_0(\psi) = \int_{-\sigma}^{0}[\sin(\omega\theta) - \sin(\omega(\theta - \tau))]w(\theta)\mathrm{d}\theta = -\frac{2\zeta\omega(\psi)}{p_{\mathrm{st}}(\psi)}$$
$$\qquad (22)$$

The D-curves in Eq. (21) can be depicted on the plane of the dimensionless angular velocity Ω and dimensionless chip width p, resulting in so-called stability lobe diagrams or stability charts. For $\Omega = 0$ and $p = 0$ no cutting takes place, hence these lines are always part of the stable region. The linear stability charts will be presented later in Fig. 4 together with the global stability boundaries.

From this point on, we investigate the Hopf bifurcation and consider the system at the stability boundary (21). For the sake of simplicity, we omit the argument ψ. We use the dimensionless chip width p as a bifurcation parameter and denote its value at the linear stability boundary by p_{st}. First, we show that there is indeed an Hopf bifurcation at the stability boundaries. For this step, we analyze the eigenvalues (or characteristic exponents) of Eq. (19), which are the roots of the characteristic function

$$D(\lambda) = \lambda^2 + 2\zeta\lambda + 1 + p\int_{-\sigma}^{0}[\mathrm{e}^{\lambda\theta} - \mathrm{e}^{\lambda(\theta - \tau)}]w(\theta)\mathrm{d}\theta \qquad (23)$$

The system is asymptotically stable if all the infinitely many eigenvalues lie in the negative half of the complex plane, whereas at the stability boundaries two eigenvalues $\lambda = \pm i\omega$ lay on the imaginary axis. The linear stability analysis reviewed in this section has already been published in Ref. [7]. In order to extend the analysis of Ref. [7], now we investigate the conditions of an Hopf bifurcation. According to Refs. [25,26], a necessary condition for an Hopf bifurcation is that the critical eigenvalues of the system cross the imaginary axis with nonzero speed as the bifurcation parameter p is increased. Hence, the real part of the critical
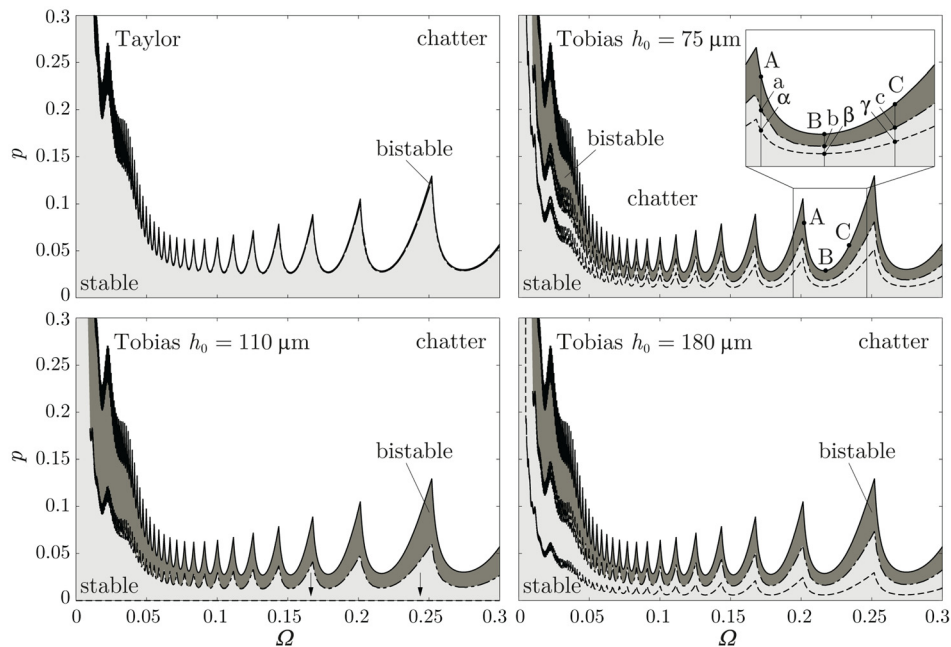

Fig. 4   Stability charts of the nonlinear turning model with cutting-force distribution (8) showing the linear stability boundaries (solid line), and the analytically estimated (dashed line) and numerically determined (dashed-dotted line) boundaries of the bistable region

characteristic exponents must change with p, which implies that the following derivative must be nonzero:

$$\gamma = \text{Re}\left[\frac{\mathrm{d}\lambda}{\mathrm{d}p}\bigg|_{\lambda=\mathrm{i}\omega}\right] = \text{Re}\left[-\left(\frac{\partial D}{\partial\lambda}\right)^{-1}\frac{\partial D}{\partial p}\bigg|_{\lambda=\mathrm{i}\omega}\right]$$

$$= -\frac{R_0 q_1 + S_0 q_2}{q_1^2 + q_2^2} = -\frac{4\pi\zeta(\omega^2+1)\omega}{p_{\text{st}}\Omega^2(q_1^2+q_2^2)}\frac{\mathrm{d}\Omega}{\mathrm{d}\psi} \quad (24)$$

where

$$q_1 = p_{\text{st}}\frac{\psi}{\omega}\frac{\mathrm{d}S_0}{\mathrm{d}\psi} + 2\zeta, \quad q_2 = -p_{\text{st}}\frac{\psi}{\omega}\frac{\mathrm{d}R_0}{\mathrm{d}\psi} + 2\omega \quad (25)$$

Consequently, an Hopf bifurcation exists when $\gamma \neq 0 \iff \mathrm{d}\Omega/\mathrm{d}\psi \neq 0$. This condition was checked numerically for each case study of this paper and it was found that $\gamma > 0$ along the stability lobes for $p_{\text{st}} > 0$. According to the Hopf bifurcation theorem, this implies that a periodic orbit exists in the vicinity of the equilibrium of the nonlinear system. In order to determine the stability and amplitude of this periodic orbit, we reduce the critical infinite-dimensional system to a finite dimensional center manifold and carry out normal form calculations in Sec. 4.

4 Center Manifold Reduction

The subsequent analysis is based on the theory of functional differential equations summarized in Ref. [27] and follows the steps of Refs. [24,28], where the orthogonal cutting model was considered with a concentrated cutting force. Note that the concentrated cutting-force model is a special case of the distributed one with Dirac delta kernel function. Now we extend the results of Refs. [24,28] and present the bifurcation analysis for a general kernel function. As the first step of the analysis, we write Eq. (16) in the first-order form

$$\mathbf{y}'(t) = \mathbf{L}\mathbf{y}(t) + \mathbf{R}\int_{-\sigma}^{0}[\mathbf{y}(t-\tau+\theta) - \mathbf{y}(t+\theta)]w(\theta)\mathrm{d}\theta + \mathbf{g}(\mathbf{y}_t)$$

$$(26)$$

where $\mathbf{y}(t)$ is the vector of state variables, $\mathbf{L}$ and $\mathbf{R}$ are the linear and the retarded coefficient matrix, and $\mathbf{g}(\mathbf{y}_t)$ contains all nonlinear terms. These quantities are defined as

$$\mathbf{y}(t) = \begin{bmatrix} \xi(t) \\ \xi'(t) \end{bmatrix}, \quad \mathbf{L} = \begin{bmatrix} 0 & 1 \\ -1 & -2\zeta \end{bmatrix}, \quad \mathbf{R} = \begin{bmatrix} 0 & 0 \\ p & 0 \end{bmatrix}$$

$$\mathbf{g}(\mathbf{y}_t) = \begin{bmatrix} 0 \\ g_2(\mathbf{y}_t) \end{bmatrix}, \quad g_2(\mathbf{y}_t) = p\int_{-\sigma}^{0}[\eta_2(y_1(t-\tau+\theta) - y_1(t+\theta))^2$$

$$+ \eta_3(y_1(t-\tau+\theta) - y_1(t+\theta))^3]w(\theta)\mathrm{d}\theta \quad (27)$$

where $y_1(t) = \xi(t)$ is the first component of $\mathbf{y}(t)$.

As the phase space of delay-differential equations is infinite-dimensional [27,29], we represent the state of the tool by $\mathbf{y}_t$ defined in the Hilbert space $\mathcal{H}$ of continuously differentiable vector valued functions: $\mathbf{y}_t \in \mathcal{H} : [-\sigma-\tau, 0] \to \mathbb{R}^2$, $\mathbf{y}_t(\vartheta) = \mathbf{y}(t+\vartheta)$. Accordingly, we characterize the evolution of the system in $\mathcal{H}$ by formulating the operator differential equation corresponding to Eq. (26)

$$\mathbf{y}_t'(\vartheta) = \mathcal{A}\mathbf{y}_t + \mathcal{F}(\mathbf{y}_t) \quad (28)$$

where $\mathcal{A}, \mathcal{F} : \mathcal{H} \to \mathcal{H}$ are the linear and the nonlinear operators, respectively

$$\mathcal{A}\mathbf{u} = \begin{cases} \mathbf{u}^{\text{o}}(\vartheta) & \text{if } \vartheta \in [-\sigma-\tau, 0) \\ \mathbf{L}\mathbf{u}(0) + \mathbf{R}\int_{-\sigma}^{0}[\mathbf{u}(\theta-\tau) - \mathbf{u}(\theta)]w(\theta)\mathrm{d}\theta & \text{if } \vartheta = 0 \end{cases}$$

$$(29)$$

$$\mathcal{F}(\mathbf{u}) = \begin{cases} 0 & \text{if } \vartheta \in [-\sigma-\tau, 0) \\ \mathbf{g}(\mathbf{u}) & \text{if } \vartheta = 0 \end{cases} \quad (30)$$

Here, the notation $\square^{\text{o}} = \mathrm{d}\square/\mathrm{d}\vartheta$ is used for the derivative with respect to ϑ.

At the stability boundaries all eigenvalues have negative real parts except the critical pair $\lambda = \pm\mathrm{i}\omega$, thus a two-dimensional critical subsystem embedded in the infinite-dimensional phase space (the so-called center manifold) attracts exponentially all the solutions of the differential equation. From a stability point of view, it is enough to study the flow on the center manifold. Therefore, we separate the center subspace from the stable one using the decomposition theorem of Ref. [27] (see Eqs. (3.10) and (3.11) in Chap. 7). By decomposing $\mathcal{H}$ with respect to the critical eigenvalues $\lambda = \pm\mathrm{i}\omega$, we can obtain a form similar to the Jordan canonical form of ordinary differential equations (see later Eq. (44)). This way a two-dimensional ordinary differential equation can be analyzed separately instead of an infinite-dimensional delayed system.

Since the center manifold is tangent to the plane spanned by the real and imaginary parts of the critical eigenfunctions (infinite-dimensional eigenvectors) of $\mathcal{A}$, we first calculate these eigenvectors, and then continue with the decomposition theorem of Ref. [27]. The critical eigenvectors $\mathbf{s}_{1,2}(\vartheta)$ are defined by

$$\mathcal{A}\mathbf{s}_{1,2}(\vartheta) = \pm\mathrm{i}\omega\mathbf{s}_{1,2}(\vartheta) \quad (31)$$

Substituting $\mathcal{A}$ from Eq. (29), writing $\mathbf{s}_{1,2}(\vartheta) = \mathbf{s}_{\text{R}}(\vartheta) \pm \mathrm{i}\mathbf{s}_{\text{I}}(\vartheta)$, and decomposing Eq. (31) into real and imaginary parts yields the boundary value problem

$$\mathbf{s}^{\text{o}}(\vartheta) = \mathbf{B}_{4\times4}\mathbf{s}(\vartheta), \quad \vartheta \in [-\sigma-\tau, 0) \quad (32)$$

$$\mathbf{L}_{4\times4}\mathbf{s}(0) + \mathbf{R}_{4\times4}\int_{-\sigma}^{0}[\mathbf{s}(\theta-\tau) - \mathbf{s}(\theta)]w(\theta)\mathrm{d}\theta = \mathbf{B}_{4\times4}\mathbf{s}(0) \quad (33)$$

where

$$\mathbf{s}(\vartheta) = \begin{bmatrix} \mathbf{s}_{\text{R}}(\vartheta) \\ \mathbf{s}_{\text{I}}(\vartheta) \end{bmatrix}, \quad \mathbf{B}_{4\times4} = \begin{bmatrix} 0 & -\omega\mathbf{I} \\ \omega\mathbf{I} & 0 \end{bmatrix}$$

$$\mathbf{L}_{4\times4} = \begin{bmatrix} \mathbf{L} & 0 \\ 0 & \mathbf{L} \end{bmatrix}, \quad \mathbf{R}_{4\times4} = \begin{bmatrix} \mathbf{R} & 0 \\ 0 & \mathbf{R} \end{bmatrix}\bigg|_{p=p_{\text{st}}} \quad (34)$$

with $\mathbf{I}$ and $\mathbf{0}$ denoting the 2×2 identity and zero matrices, respectively. The solution of Eq. (32) has the form $\mathbf{s}(\vartheta) = \mathrm{e}^{\mathbf{B}_{4\times4}\vartheta}\mathbf{c}$. The constant $\mathbf{c} = [c_{11}\, c_{12}\, c_{21}\, c_{22}]^{\text{T}}$ can be determined from Eq. (33). With the arbitrary choice $c_{11} = 1$ and $c_{21} = 0$, we get

$$\mathbf{s}_{\text{R}}(\vartheta) = \begin{bmatrix} \cos(\omega\vartheta) \\ -\omega\sin(\omega\vartheta) \end{bmatrix}, \quad \mathbf{s}_{\text{I}}(\vartheta) = \begin{bmatrix} \sin(\omega\vartheta) \\ \omega\cos(\omega\vartheta) \end{bmatrix} \quad (35)$$

The decomposition theorem of Ref. [27] also uses the so-called left eigenvectors, which are the eigenvectors of the operator $\mathcal{A}^{\text{H}}$ being formally adjoint to $\mathcal{A}$ relative to a certain bilinear form. The formal adjoint $\mathcal{A}^{\text{H}} : \mathcal{H}^{\text{H}} \to \mathcal{H}^{\text{H}}$ must satisfy

$$(\mathbf{v}, \mathcal{A}\mathbf{u}) = (\mathcal{A}^{\text{H}}\mathbf{v}, \mathbf{u}) \quad (36)$$

where $\mathbf{u} \in \mathcal{H} : [-\sigma-\tau, 0] \to \mathbb{R}^2$ and $\mathbf{v} \in \mathcal{H}^{\text{H}} : [0, \sigma+\tau] \to \mathbb{R}^2$, $\mathcal{H}^{\text{H}}$ is the adjoint space. The operation $(,) : \mathcal{H}^{\text{H}} \times \mathcal{H} \to \mathbb{R}$ indicates the bilinear form. The definition of the formal adjoint and the bilinear form can be found in Ref. [27] (see Eqs. (3.1) and (3.3) in Chap. 7), and here they read

$$
\mathcal{A}^H \mathbf{v} =
\begin{cases}
-\mathbf{v}^o(\vartheta) & \text{if } \vartheta \in (0, \sigma + \tau] \\
\mathbf{L}^H \mathbf{v}(0) + \mathbf{R}^H \displaystyle\int_{-\sigma}^{0} [\mathbf{v}(\tau - \theta) - \mathbf{v}(-\theta)] w(\theta) \mathrm{d}\theta & \\
& \text{if } \vartheta = 0
\end{cases}
\tag{37}
$$

$$
(\mathbf{u}, \mathbf{v}) = \mathbf{u}^H(0)\mathbf{v}(0) + \int_{-\sigma}^{0}\int_{-\theta}^{0} \mathbf{u}^H(\vartheta)(\mathbf{R}w(\theta))\mathbf{v}(\vartheta + \theta)\mathrm{d}\vartheta\mathrm{d}\theta \\
- \int_{-\sigma-\tau}^{-\tau}\int_{-\theta}^{0} \mathbf{u}^H(\vartheta)(\mathbf{R}w(\tau + \theta))\mathbf{v}(\vartheta + \theta)\mathrm{d}\vartheta\mathrm{d}\theta
\tag{38}
$$

where the superscript H of $\mathbf{R}$, $\mathbf{L}$, and $\mathbf{u}$ refers to conjugate transpose.

As the eigenvalues of $\mathcal{A}^H$ are complex conjugates to those of $\mathcal{A}$, the left eigenvectors $\mathbf{n}_{1,2}(\varphi)$ satisfy

$$
\mathcal{A}^H \mathbf{n}_{1,2}(\varphi) = \mp \mathrm{i}\omega\mathbf{n}_{1,2}(\varphi)
\tag{39}
$$

We determine $\mathbf{n}_{1,2}(\varphi) = \mathbf{n}_R(\varphi) \pm \mathrm{i}\mathbf{n}_I(\varphi)$ the same way as we computed $\mathbf{s}_{1,2}(\varphi)$. This time, however, we cannot choose the coefficients of $\mathbf{n}_{R,I}(\varphi)$ arbitrarily as we did for $\mathbf{s}_{R,I}(\vartheta)$ by taking $c_{11} = 1$ and $c_{21} = 0$, because, in order to apply the decomposition theorem of Ref. [27], the following orthonormality condition must be satisfied:

$$
(\mathbf{n}_R, \mathbf{s}_R) = 1, \quad (\mathbf{n}_R, \mathbf{s}_I) = 0
\tag{40}
$$

Finally, we get the left eigenfunctions in the form

$$
\mathbf{n}_R(\varphi) = \frac{2}{q_1^2 + q_2^2}
\begin{bmatrix}
(2\zeta q_1 + \omega q_2)\cos(\omega\varphi) + (\omega q_1 - 2\zeta q_2)\sin(\omega\varphi) \\
q_1\cos(\omega\varphi) - q_2\sin(\omega\varphi)
\end{bmatrix}
$$
$$
\mathbf{n}_I(\varphi) = \frac{2}{q_1^2 + q_2^2}
\begin{bmatrix}
(-\omega q_1 + 2\zeta q_2)\cos(\omega\varphi) + (2\zeta q_1 + \omega q_2)\sin(\omega\varphi) \\
q_2\cos(\omega\varphi) + q_1\sin(\omega\varphi)
\end{bmatrix}
\tag{41}
$$

According to Ref. [27], we decompose the solution space as

$$
\mathbf{y}_t(\vartheta) = z_1(t)\mathbf{s}_R(\vartheta) + z_2(t)\mathbf{s}_I(\vartheta) + \mathbf{y}_m(t)(\vartheta)
\tag{42}
$$

where $z_1(t)$ and $z_2(t)$ are local coordinates on the center manifold introduced to describe the behavior of the critical subsystem, whereas $\mathbf{y}_m(t)$ accounts for the remaining infinite-dimensional subsystem with coordinates perpendicular to the center manifold. The decomposition theorem gives the formula of the different components

$$
z_1(t) = (\mathbf{n}_R, \mathbf{y}_t)
$$
$$
z_2(t) = (\mathbf{n}_I, \mathbf{y}_t)
\tag{43}
$$
$$
\mathbf{y}_m(t)(\vartheta) = \mathbf{y}_t(\vartheta) - z_1(t)\mathbf{s}_R(\vartheta) - z_2(t)\mathbf{s}_I(\vartheta)
$$

Differentiating these expressions with respect to time and using Eqs. (28), (42), and (31), the following differential equation can be obtained:

$$
\begin{bmatrix} z_1' \\ z_2' \\ \mathbf{y}_{tn}' \end{bmatrix} =
\begin{bmatrix} 0 & \omega & \mathcal{O} \\ -\omega & 0 & \mathcal{O} \\ \mathscr{O} & \mathscr{O} & \mathcal{A} \end{bmatrix}
\begin{bmatrix} z_1 \\ z_2 \\ \mathbf{y}_{tn} \end{bmatrix}
$$
$$
+ \begin{bmatrix}
n_{R2}(0)\mathcal{F}_2(0) \\
n_{I2}(0)\mathcal{F}_2(0) \\
-n_{R2}(0)\mathcal{F}_2(0)\mathbf{s}_R - n_{I2}(0)\mathcal{F}_2(0)\mathbf{s}_I + \mathcal{F}
\end{bmatrix}
\tag{44}
$$

where $\mathcal{O} : \mathbb{R} \to \mathcal{H}$ and $\mathscr{O} : \mathcal{H} \to \mathbb{R}$ are zero operators, and subscript 2 indicates the second component of vectors.

Note that the two-dimensional critical subsystem is decoupled linearly in Eq. (44), but there is still a coupling through the

nonlinear term $\mathcal{F}_2(0)$. In order to fully decouple the critical subsystem and to obtain it in a third-order normal form, $\mathcal{F}_2(0)$ should be expressed in terms of z_1 and z_2 up to third order, which requires a second-order approximation of the center manifold itself

$$
\mathbf{y}_m(\vartheta) = \frac{1}{2}\left[\mathbf{h}_1(\vartheta)z_1^2 + 2\mathbf{h}_2(\vartheta)z_1 z_2 + \mathbf{h}_3(\vartheta)z_2^2\right]
\tag{45}
$$

The coefficients $\mathbf{h}_1(\vartheta)$, $\mathbf{h}_2(\vartheta)$, and $\mathbf{h}_3(\vartheta)$ can be calculated as follows. First we differentiate Eq. (45) with respect to time and substitute the rows of Eq. (42) to express the temporal derivatives. Then, we consider the case $\vartheta \in [-\sigma - \tau, 0)$ and substitute the definitions (29) and (30) of $\mathcal{A}$ and $\mathcal{F}$ accordingly. We also substitute the derivative of Eq. (45) with respect to ϑ. Thereafter, we use a second-order approximation of $\mathcal{F}_2(0)$ as

$$
\mathcal{F}_2(0) \approx F_1 z_1^2 + F_2 z_1 z_2 + F_3 z_2^2
\tag{46}
$$

Finally, we collect the coefficients of the second-order terms of z_1 and z_2 and consider a polynomial balance. This way we end up with the differential equation

$$
\mathbf{h}^o(\vartheta) = \mathbf{C}_{6\times6}\mathbf{h}(\vartheta) + \mathbf{p}\cos(\omega\vartheta) + \mathbf{q}\sin(\omega\vartheta)
\tag{47}
$$

where

$$
\mathbf{h}(\vartheta) = \begin{bmatrix} \mathbf{h}_1(\vartheta) \\ \mathbf{h}_2(\vartheta) \\ \mathbf{h}_3(\vartheta) \end{bmatrix}, \quad
\mathbf{C}_{6\times6} = \begin{bmatrix} 0 & -2\omega\mathbf{I} & 0 \\ \omega\mathbf{I} & 0 & -\omega\mathbf{I} \\ 0 & 2\omega\mathbf{I} & 0 \end{bmatrix}
$$

$$
\mathbf{p} = \frac{2}{q_1^2 + q_2^2}\begin{bmatrix} 2q_1 F_1 \\ 2q_2\omega F_1 \\ q_1 F_2 \\ q_2\omega F_2 \\ 2q_1 F_3 \\ 2q_2\omega F_3 \end{bmatrix}, \quad
\mathbf{q} = \frac{2}{q_1^2 + q_2^2}\begin{bmatrix} 2q_2 F_1 \\ -2q_1\omega F_1 \\ q_2 F_2 \\ -q_1\omega F_2 \\ 2q_2 F_3 \\ -2q_1\omega F_3 \end{bmatrix}
\tag{48}
$$

The solution of Eq. (47) is of the form

$$
\mathbf{h}(\vartheta) = \mathbf{M}\cos(\omega\vartheta) + \mathbf{N}\sin(\omega\vartheta) + e^{\mathbf{C}_{6\times6}\vartheta}\mathbf{K}
\tag{49}
$$

Matrices $\mathbf{M}$ and $\mathbf{N}$ can be obtained by substituting the trial solution (49) back into Eq. (47) and considering a harmonic balance. In order to calculate $\mathbf{K}$, we return to Eq. (45), differentiate it with respect to time, and substitute the rows of Eq. (42) as before. This time, however, we consider $\vartheta = 0$, and substitute the definitions (29) and (30) of $\mathcal{A}$ and $\mathcal{F}$ accordingly. Using the second-order approximation (46), a polynomial balance of the second-order terms of z_1 and z_2 yields the boundary condition

$$
\mathbf{P}_{6\times6}\mathbf{h}(0) + \mathbf{R}_{6\times6}\int_{-\sigma}^{0}[\mathbf{h}(\theta - \tau) - \mathbf{h}(\theta)]w(\theta)\mathrm{d}\theta = \mathbf{p} + \mathbf{r}
\tag{50}
$$

where

$$
\mathbf{R}_{6\times6} = \begin{bmatrix} \mathbf{R} & 0 & 0 \\ 0 & \mathbf{R} & 0 \\ 0 & 0 & \mathbf{R} \end{bmatrix}, \quad
\mathbf{L}_{6\times6} = \begin{bmatrix} \mathbf{L} & 0 & 0 \\ 0 & \mathbf{L} & 0 \\ 0 & 0 & \mathbf{L} \end{bmatrix}
$$

$$
\mathbf{P}_{6\times6} = \mathbf{L}_{6\times6} - \mathbf{C}_{6\times6}, \quad \mathbf{r} = -\begin{bmatrix} 0 & 2F_1 & 0 & F_2 & 0 & 2F_3 \end{bmatrix}^T
\tag{51}
$$

After substituting the trial solution (49) into the boundary condition (50) we can find $\mathbf{K}$. Then, the coefficients $\mathbf{h}_1(\vartheta)$, $\mathbf{h}_2(\vartheta)$, and $\mathbf{h}_3(\vartheta)$ can be given according to Eq. (49), where the second-order approximation (45) of the center manifold is obtained.

Using Eqs. (42) and (45), we can obtain a third-order approximation of the nonlinear terms in the first two rows of Eq. (44), where we get the critical subsystem in the third-order normal form

$$
\begin{bmatrix} z_1' \\ z_2' \end{bmatrix} = \begin{bmatrix} 0 & \omega \\ -\omega & 0 \end{bmatrix} \begin{bmatrix} z_1 \\ z_2 \end{bmatrix} + \begin{bmatrix} \sum_{j+k=2,3} a_{jk} z_1^j z_2^k \\ \sum_{j+k=2,3} b_{jk} z_1^j z_2^k \end{bmatrix} \quad (52)
$$

Thereafter, the bifurcation analysis and the calculation of periodic orbits can be performed on the two-dimensional system (52) instead of the infinite-dimensional one (28).

5 Estimation of the Bistable Region

We can determine the criticality of the Hopf bifurcation, that is, the stability of periodic orbits, based on the sign of the Poincaré–Lyapunov constant (PLC) given by [25]

$$
\Delta = \frac{1}{8\omega} \Big[(a_{20} + a_{02})(-a_{11} + b_{20} - b_{02}) \\
+ (b_{20} + b_{02})(b_{11} + a_{20} - a_{02}) \Big] \\
+ \frac{1}{8}(3a_{30} + a_{12} + b_{21} + 3b_{03}) \quad (53)
$$

which gives

$$
\Delta = \frac{(1 - \cos\psi)p_{\text{st}}\gamma}{2}\left(3\eta_3 - \delta\eta_2^2\right) \quad (54)
$$

$$
\delta = 1 - \frac{S_0 q_1 - R_0 q_2}{-R_0 q_1 - S_0 q_2}\Big[2p_{\text{st}}\big(4\zeta\omega R_{02} + (4\omega^2 - 1)S_{02}\big) \\
+ p_{\text{st}}^2\big(R_{02}^2 + S_{02}^2\big) - (4\omega^2 - 1)^2 - (4\zeta\omega)^2\Big] \\
\times \frac{1}{\left[p_{\text{st}}R_{02} - (4\omega^2 - 1)\right]^2 + \left[p_{\text{st}}S_{02} + 4\zeta\omega\right]^2} \quad (55)
$$

where $R_{02}(\psi) = R_0(2\psi)$ and $S_{02}(\psi) = S_0(2\psi)$.

The bifurcation is subcritical when the PLC is positive and supercritical when it is negative. It was shown in Ref. [24] that the Hopf bifurcation is subcritical for the special case of concentrated cutting force with Dirac delta kernel. Here, we determined the PLC numerically for several case studies by plotting $\Delta(\psi)$. We encountered no supercritical case, which indicates that the subcritical nature of machining processes is preserved for realistic cutting-force distributions.

The subcritical Hopf bifurcation gives rise to an unstable periodic orbit around the linearly stable equilibrium, hence the equilibrium has a finite domain of attraction. Once a perturbation (e.g., material inhomogeneity, external excitation) moves the system out of this domain, the resulting vibrations do not settle down, but grow in amplitude until the tool leaves the workpiece material resulting in chatter. Outside the cut the tool undergoes a damped free oscillation, which limits the chatter amplitude, and the tool gets back to the workpiece again. Hence, the large-amplitude chatter with loss of contact is stable in the dynamical sense [7]. Therefore, for certain set of parameters, stationary cutting and large-amplitude chatter coexist. This parameter domain is referred to as the region of bistability or unsafe zone.

In the bistable region, the amplitude of the arising periodic orbit can be approximated [26] by

$$
r(\psi, p) \approx \sqrt{-\frac{\gamma(\psi)}{\Delta(\psi)}(p - p_{\text{st}}(\psi))} \quad (56)
$$

It is important to emphasize the difference between the actual bifurcation parameter value p and the stability limit $p_{\text{st}}(\psi)$. The

corresponding approximate periodic orbit and tool position become

$$
\mathbf{y}_t(\vartheta) \approx r(\psi, p)[\cos(\omega t)\mathbf{s}_R(\vartheta) - \sin(\omega t)\mathbf{s}_I(\vartheta)] \quad (57)
$$

$$
\xi(t) = y_1(t) = y_{t1}(0) \approx r(\psi, p)\cos(\omega t) \quad (58)
$$

The unstable limit cycle exists only if the tool does not lose contact with the workpiece during chatter. Once the amplitude of the periodic orbit gets so large that loss of contact occurs, the unstable periodic orbit vanishes as Eq. (16) is no longer valid. Consequently, the region of bistability is limited by the so-called switching line where the tool just loses contact with the workpiece, that is, where the chip thickness $h(t, \theta)$ drops to zero. Note that this statement could be verified by the analysis of the nonsmooth system involving loss of contact between tool and workpiece. The analysis of the nonsmooth dynamics, where also the second row of Eq. (5) or (6) is taken into account, is out of scope of this paper. We rely on the results of Ref. [30] where it was shown for a concentrated cutting-force model that the boundary of the bistable region is indeed given by the case where the unstable periodic orbit touches the switching line. The dimensionless form of Eq. (10) yields the switching condition

$$
1 + \xi(t - \tau + \theta) - \xi(t + \theta) = 0 \quad (59)
$$

Substituting the periodic solution (58), the switching condition can be written in the form

$$
1 = r(\psi, p)\sqrt{(1 - \cos\psi)^2 + \sin^2\psi}\cos(\omega(t + \theta) + \phi) \quad (60)
$$

where ϕ is a phase shift. If there exists any pair of t and θ such that the switching condition is fulfilled, then loss of contact happens and the periodic orbit disappears. In order to find the smallest amplitude for which $h(t, \theta) = 0$ occurs, we write $\cos(\omega(t + \theta) + \phi) = 1$. Substituting the approximate amplitude (56) and rearranging Eq. (60) for p, we get the boundary of the bistable region in the form

$$
p_{\text{bist}}(\psi) = -\frac{1}{2}\frac{\Delta(\psi)}{\gamma(\psi)}\frac{1}{1 - \cos\psi} + p_{\text{st}}(\psi) \quad (61)
$$

Therefore, the system is linearly but not globally stable (unsafe) for $p_{\text{bist}}(\psi) \leq p < p_{\text{st}}(\psi)$, and it is globally stable for $0 \leq p < p_{\text{bist}}(\psi)$. The stability boundaries $p_{\text{st}}(\psi)$ and $p_{\text{bist}}(\psi)$ are shown in Fig. 4 together with their numerically computed counterparts.

6 Numerical Analysis

It is important to highlight that formulas (56)–(58) are approximations, thus Eq. (61) serves only as an estimation for the size of the bistable region. In order to verify the accuracy of these results, we analyze the stability of system (16) numerically using the continuation software DDE-BIFTOOL [9,10].

As a first step, we rescale Eq. (16) by introducing the scaled time T such that $t = T\tau$. This step is necessary to avoid a badly scaled system for small Ω, when $\tau \to \infty$. Using T, Eq. (16) can be written in the form

$$
\xi''(T) + 2\zeta\tau\xi'(T) + \tau^2\xi(T) \\
= p\tau^2 \int_{-\varepsilon}^{0} [(\xi(T - 1 + \eta) - \xi(T + \eta)) \\
+ \eta_2(\xi(T - 1 + \eta) - \xi(T + \eta))^2 \\
+ \eta_3(\xi(T - 1 + \eta) - \xi(T + \eta))^3]\tau w(\tau\eta)\mathrm{d}\eta \quad (62)
$$

where $\eta = \theta/\tau$ and prime now denotes the derivative with respect to T. Note that in Eq. (62) the delay is limited to a finite value even when $\tau \to \infty$.

To use DDE-BIFTOOL, we approximate the distributed delay term by a sum of f point delays as follows:

$$\xi''(T) + 2\zeta\tau\xi'(T) + \tau^2\xi(T)$$
$$\approx p\tau^2\sum_{k=1}^{f}\Big[(\xi(T-1-\hat{\eta}_k)-\xi(T-\hat{\eta}_k))$$
$$+\eta_2(\xi(T-1-\hat{\eta}_k)-\xi(T-\hat{\eta}_k))^2$$
$$+\eta_3(\xi(T-1-\hat{\eta}_k)-\xi(T-\hat{\eta}_k))^3\Big]w_k \qquad (63)$$

where

$$\hat{\eta}_k = \left(k-\frac{1}{2}\right)\frac{\varepsilon}{f}, \quad w_k = \int_{-k\varepsilon/f}^{-(k-1)\varepsilon/f}\tau w(\tau\eta)\mathrm{d}\eta \qquad (64)$$

$k = 1,\ldots,f$. Note that the term $\tau w(\tau\eta)$ is independent of τ, therefore it is enough to calculate w_k (and also $\hat{\eta}_k$) once, their values do not change during the numerical continuation. For the numerical calculations we used $f = 20$, which provided the linear stability boundaries with accuracy within linewidth.

We implemented Eq. (63) in DDE-BIFTOOL, and used numerical continuation to determine the stability boundaries where the Hopf bifurcation occurs. In each point of the boundaries, we computed the amplitude of the arising periodic orbit by fixing Ω and varying p. We also determined the corresponding periodic orbit itself, and checked the switching condition (59) in a form scaled to T. Using Newton's method, we iterated the value of the bifurcation parameter p until the switching condition was fulfilled. This way, we determined the corresponding bistable limit for each point of the Hopf stability boundaries. The analytical and numerical results are summarized in Sec. 7.

7 Results and Discussion

Figure 4 shows a series of stability charts with the linearly and globally stable parameter regions assuming $\zeta = 0.02$, $\varepsilon = 0.05$, and $\alpha = 0.4$. Four cases are considered: the Taylor force model and the Tobias force expression with $h_0 = 75, 110, 180\,\mu m$. The linear stability boundary at $p = p_{st}(\psi)$, where the Hopf bifurcation occurs, is indicated by solid line. The boundary $p = p_{bist}(\psi)$ of the bistable region according to the analytical estimation (61) is shown by a dashed line, whereas its numerically computed counterpart is denoted by dashed-dotted line. Note that in the top left chart of the figure the dashed and dashed-dotted lines overlap, whereas in the bottom left chart the dashed boundary flips to the half plane $p < 0$.

It is known that the minima of the linear stability lobes lie on a line $p = $ constant for concentrated cutting force, see, e.g., Ref. [31]. However, as shown in Fig. 4, it is not the case for the distributed cutting-force model, where the stability lobes shift upward in case of low spindle speeds. Furthermore, the size of the bistable region grows when the linearly stable region also does. Therefore, we express the size of the bistable region relative to the size of the linearly stable region

$$\Delta p(\psi) = \frac{p_{st}(\psi) - p_{bist}(\psi)}{p_{st}(\psi)} = \frac{3}{4}\eta_3 - \frac{1}{4}\delta(\psi)\eta_2^2 \qquad (65)$$

Investigating the parameter ranges $\zeta = 0.001$–0.2 and $\varepsilon = 0.001$–0.2, we found that the magnitude of $|\delta(\psi)|$ is around 10^{-5} to 10^{-2} irrespective of the kernel shape given by $\alpha = 0$–1. Thus, the term $\delta(\psi)\eta_2^2$ is negligible compared to $3\eta_3$, and we end up with a very simple analytical estimate for the size of the bistable region

$$\Delta p_{est} = \frac{3}{4}\eta_3 = \frac{3\rho_3 h_0^2}{4\rho_1 + 8\rho_2 h_0 + 12\rho_3 h_0^2} \qquad (66)$$

Note that after omitting $\delta(\psi)$, we get the same size for the bistable region irrespective of both the spindle speed Ω and the shape $w(\theta)$

of the cutting-force distribution. Consequently, the same estimation works for concentrated cutting-force models as well, which was also shown in Ref. [16].

In the case of the Taylor force ($\eta_3 = 5/96$), the formula gives $\Delta p_{est} = 0.039$. It is in good agreement with Refs. [24,28], where the size of the bistable region was shown to be 4% at the notches of the lobes for concentrated cutting force. In the case of the Tobias force, the size of the bistable region depends on the mean chip thickness h_0 as shown in Fig. 5. Here, the analytical estimate (66) is indicated by dashed line. We can see that Δp_{est} peaks at a critical mean chip thickness h_{cr}, and tends to 25% for large h_0. According to Ref. [24], the critical mean chip thickness is $h_{cr} = -\rho_1/\rho_2 = 113\,\mu m$. Around h_{cr} the size of the bistable region exceeds 100%, which shows that here the analytical estimation loses accuracy, since formula (56) for the amplitude of periodic orbits is valid only in the vicinity of the linear stability boundaries. Therefore, we computed the size of the bistable region numerically by DDE-BIFTOOL for several mean chip thickness values h_0, see the dots in Fig. 5. In the numerical analysis, we still found that the size of the bistable region relative to the size of the linearly stable region is approximately constant along the stability lobes for a fixed h_0. The dots of Fig. 5 indicate the average size along the second lobe as function of the mean chip thickness h_0. It can be seen that the location h_{cr} of the peak remains the same, and the limit value for large h_0 is about 20%. We can also conclude that the analytical estimation (66) gives good approximation only for small mean chip thickness values ($h_0 \lesssim 60\,\mu m$).

Finally, we explain the difference between the analytical and numerical results in Fig. 6. Here, the amplitude of periodic orbits
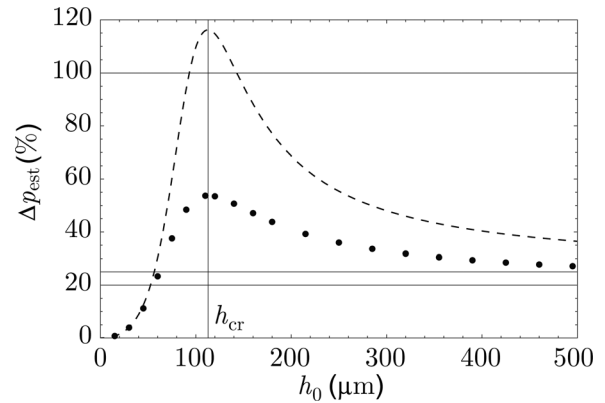
Fig. 5 Ratio of the size of the bistable region and the linearly stable region assuming Tobias force (dashed line: analytical estimate, dots: numerical results)
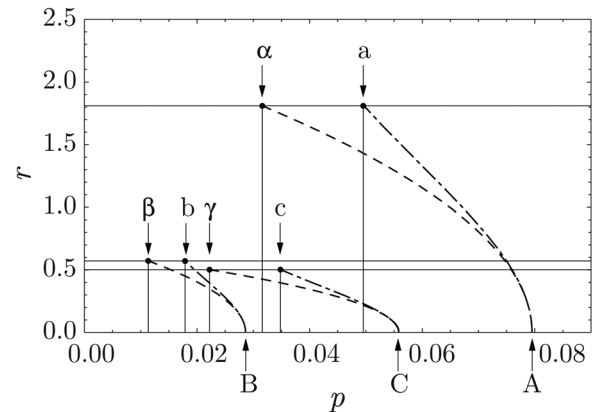
Fig. 6 Bifurcation diagram showing the amplitude of periodic orbits in the vicinity of the parameter points A, B, and C in Fig. 4 (dashed line: analytical estimate, dashed-dotted line: numerical result)

is presented in the vicinity of the parameter points A ($\Omega = 0.2025$, $p = 0.0795$), B ($\Omega = 0.2171$, $p = 0.0286$), and C ($\Omega = 0.2343$, $p = 0.0558$) in the top right panel of Fig. 4. The analytical estimate (56) is indicated by dashed line, its numerical counterpart is denoted by dash-dot line. We can see that near the linear stability boundaries at A, B, and C the analytical and numerical bifurcation curves overlap. However, further away from A, B, and C, the curves deviate as the amplitude cannot be approximated accurately by the square-root function (56). The inaccuracy of the estimate (56) can be explained as follows. For $p = 0$, the right-hand side of the governing equation (16) disappears, and the system reduces to a damped oscillator, which cannot exhibit periodic solutions. Therefore, the bifurcation curves should not cross the line $p = 0$. This property is clearly not satisfied by the square-root function in Eq. (56). On the other hand, the numerical results show that the amplitude r of the periodic solutions tends to infinity as $p \to 0$, i.e., no periodic solution is possible at $p = 0$. The smallest amplitude where the switching condition is fulfilled is shown by a horizontal line. The points where the bifurcation curves cross the horizontal lines are indicated by α, β, γ, and a, b, c in the analytical and numerical case, respectively. The difference between the analytical estimation and the numerical results becomes large if these points lie far from the linear stability boundaries, that is, when the bistable region is large. Note that beyond these points the bifurcation curves are not depicted, since they are not valid as loss of contact occurs between the tool and the workpiece.

8 Conclusions

We can conclude that the cutting-force distribution along the tool's rake face has an important effect on the stability of the machining process: it increases the linearly stable region at small spindle speeds. Therefore, this so-called short regenerative effect allows chatter-free operation for larger depth of cut, by which the material removal rate of low-speed cutting processes can be improved. Mathematically, the short regenerative effect is represented by a distributed delay term in the governing equations of the system, where a short distributed delay is superimposed on the regenerative delay. The added delay accounts for the seemingly unimportant fact that the chip needs a certain amount of time to slip along the tool's rake face. Both analytical estimations and numerical results show that such a small effect makes qualitative changes in the dynamic behavior of the system.

Moreover, through the analytical and numerical bifurcation analysis of the governing delay-differential equation with distributed delay, we have shown that orthogonal cutting processes are subcritical for realistic cutting-force distributions even at small cutting speeds where the distributed nature of the cutting force is relevant. No formal proof was given for the existence of an Hopf bifurcation and for its subcritical sense; however, the crossing speed of the characteristic exponents and the PLC has been derived analytically, and their values were evaluated numerically for several parameter combinations. All the numerical results verified the existence of a subcritical Hopf bifurcation.

Accordingly, there exists a bistable region near the linear stability boundaries, where stable stationary cutting and large-amplitude chatter coexist. The size of the bistable region depends on the characteristics of the cutting force. If the cutting-force characteristics is given by a power law (Taylor force), then the bistable region is thin, it occupies only 4% of the linearly stable region, and its size does not depend on the feed h_0 per revolution. The bistable region is significantly larger and is feed-dependent for a cubic cutting-force characteristics (Tobias force). The existence of an inflection point in the cubic characteristics ($\rho_2 < 0$) further increases the size of the bistable region, see Eq. (66). Nevertheless, as the boundary of the bistable region follows the linear stability boundary, it is still reasonable to operate the system in one of the peaks of the linear stability lobe diagrams. Besides, in the case of inflected cutting-force characteristics, the size of the bistable region peaks for a critical feed per revolution.

Therefore, this feed per revolution range should be avoided in order to decrease the possibility of large-amplitude vibrations within the linearly stable parameter region.

Finally, note that uncertainties in the parameters of the cutting force magnitude and distribution affect both the linear stability boundaries and the size of the bistable region. Therefore, the accuracy of the analysis depends on the accuracy of the parameters in the cutting-force model, and the results are valid only for narrow spindle speed ranges where these parameters do not change significantly.

References

[1] Tobias, S. A., and Fishwick, W., 1958, "Theory of Regenerative Machine Tool Chatter," Engineer, **205**, pp. 199–203; 238–239.
[2] Tlusty, J., and Polacek, M., 1963, "The Stability of the Machine Tool Against Self-Excited Vibration in Machining," ASME Production Engineering Research Conference, pp. 454–465.
[3] Clancy, B. E., and Shin, Y. C., 2002, "A Comprehensive Chatter Prediction Model for Face Turning Operation Including Tool Wear Effect," Int. J. Mach. Tools Manuf., **42**(9), pp. 1035–1044.
[4] Ahmadi, K., and Ismail, F., 2010, "Experimental Investigation of Process Damping Nonlinearity in Machining Chatter," Int. J. Mach. Tools Manuf., **50**(11), pp. 1006–1014.
[5] Shi, Y., Mahr, F., von Wagner, U., and Uhlmann, E., 2012, "Chatter Frequencies of Micromilling Processes: Influencing Factors and Online Detection Via Piezoactuators," Int. J. Mach. Tools Manuf., **56**, pp. 10–16.
[6] Altintas, Y., 2012, *Manufacturing Automation—Metal Cutting Mechanics, Machine Tool Vibrations and CNC Design*, 2nd ed., Cambridge University Press, Cambridge, MA.
[7] Stépán, G., 1997, "Delay-Differential Equation Models for Machine Tool Chatter," *Dynamics and Chaos in Manufacturing Processes*, F. C. Moon, ed., Wiley, New York, pp. 165–192.
[8] Molnár, T. G., and Insperger, T., 2015, "On the Effect of Distributed Regenerative Delay on the Stability Lobe Diagrams of Milling Processes," Period. Polytech., Mech. Eng., **59**(3), pp. 126–136.
[9] Engelborghs, K., Luzyanina, T., and Roose, D., 2002, "Numerical Bifurcation Analysis of Delay Differential Equations Using DDE-BIFTOOL," ACM Trans. Math. Software, **28**(1), pp. 1–21.
[10] Sieber, J., Engelborghs, K., Luzyanina, T., Samaey, G., and Roose, D., 2014, "DDE-BIFTOOL v. 3.0 Manual—Bifurcation Analysis of Delay Differential Equations," http://arxiv.org/abs/1406.7144.
[11] Barrow, G., Graham, W., Kurimoto, T., and Leong, Y. F., 1982, "Determination of Rake Face Stress Distribution in Orthogonal Machining," Int. J. Mach. Tool Des. Res., **22**(1), pp. 75–85.
[12] Buryta, D., Sowerby, R., and Yellowley, I., 1994, "Stress Distributions on the Rake Face During Orthogonal Machining," Int. J. Mach. Tools Manuf., **34**(5), pp. 721–739.
[13] Bagchi, A., and Wright, P. K., 1987, "Stress Analysis in Machining With the Use of Sapphire Tools," Proc. R. Soc. London, Ser. A, **409**(1836), pp. 99–113.
[14] Taylor, F. W., 1907, *On the Art of Cutting Metals*, ASME, New York.
[15] Shi, H. M., and Tobias, S. A., 1984, "Theory of Finite Amplitude Machine Tool Instability," Int. J. Mach. Tool Des. Res., **24**(1), pp. 45–69.
[16] Stépán, G., Dombóvári, Z., and Muñoa, J., 2011, "Identification of Cutting Force Characteristics Based on Chatter Experiments," CIRP Ann. Manuf. Technol., **60**(1), pp. 113–116.
[17] Yang, X., and Liu, C. R., 2002, "A New Stress-Based Model of Friction Behavior in Machining and Its Significant Impact on Residual Stresses Computed by Finite Element Method," Int. J. Mech. Sci., **44**(4), pp. 703–723.
[18] Astakhov, V. P., and Outeiro, J. C., 2005, "Modeling of the Contact Stress Distribution at the Tool–Chip Interface," Mach. Sci. Technol., **9**(1), pp. 85–99.
[19] Kilic, D. S., and Raman, S., 2007, "Observations of the Tool–Chip Boundary Conditions in Turning of Aluminum Alloys," Wear, **262**(7–8), pp. 889–904.
[20] Kato, S., Yamaguchi, K., and Yamada, M., 1972, "Stress Distribution at the Interface Between Tool and Chip in Machining," ASME J. Eng. Ind., **94**(2), pp. 683–689.
[21] Childs, T. H. C., and Mahdi, M. I., 1989, "On the Stress Distribution Between the Chip and Tool During Metal Turning," CIRP Ann. Manuf. Technol., **38**(1), pp. 55–58.
[22] Chandrasekaran, H., and Kapoor, D. V., 1965, "Photoelastic Analysis of Chip–Tool Interface Stresses," ASME J. Eng. Ind., **87**(4), pp. 495–502.

[23] Woon, K. S., Rahman, M., Neo, K. S., and Liu, K., 2008, "The Effect of Tool Edge Radius on the Contact Phenomenon of Tool-Based Micromachining," Int. J. Mach. Tools Manuf., **48**(12–13), pp. 1395–1407.

[24] Dombóvári, Z., Wilson, R. E., and Stépán, G., 2008, "Estimates of the Bistable Region in Metal Cutting," Proc. R. Soc. A, **464**(2100), pp. 3255–3271.

[25] Hassard, B. D., Kazarinoff, N. D., and Wan, Y.-H., 1981, *Theory and Applications of Hopf Bifurcation* (London Mathematical Society Lecture Note Series), Vol. 41, Cambridge University Press, Cambridge, UK.

[26] Guckenheimer, J., and Holmes, P., 1983, *Nonlinear Oscillations, Dynamical Systems, and Bifurcations of Vector Fields*, Springer, New York.

[27] Hale, J., 1977, *Theory of Functional Differential Equations*, Springer, New York.

[28] Stépán, G., and Kalmár-Nagy, T., 1997, "Nonlinear Regenerative Machine Tool Vibrations," Proceedings of DETC'97, ASME Design and Technical Conferences, pp. 1–11.

[29] Stépán, G., 1989, *Retarded Dynamical Systems*, Longman, Harlow, UK.

[30] Dombóvári, Z., Barton, D. A., Wilson, R. E., and Stépán, G., 2011, "On the Global Dynamics of Chatter in the Orthogonal Cutting Model," Int. J. Nonlinear Mech., **46**(1), pp. 330–338.

[31] Insperger, T., and Stépán, G., 2011, *Semi-Discretization for Time-Delay Systems—Stability and Engineering Applications*, Springer, New York.